Nucleation and Growth of Graphite in Eutectic Spheroidal Cast Iron: Modeling and Testing

FERNANDO D. CARAZO, PATRICIA M. DARDATI, DIEGO J. CELENTANO, and LUIS A. GODOY

A new model of graphite growth during the continuous cooling of eutectic spheroidal cast iron is presented in this paper. The model considers the nucleation and growth of graphite from pouring to room temperature. The microstructural model of solidification accounts for the eutectic as divorced and graphite growth rate as a function of carbon gradient at the liquid in contact with the graphite. In the solid state, the microstructural model takes into account three stages for graphite growth, namely (1) from the end of solidification to the upper bound of intercritical stable eutectoid, (2) during the intercritical stable eutectoid, and (3) from the lower bound of intercritical stable eutectoid to room temperature. The micro- and macrostructural models are coupled using a sequential multiscale approach. Numerical results for graphite fraction and size distribution are compared with experimental results obtained from a cylindrical cup, in which the graphite volumetric fraction and size distribution were obtained using the Schwartz–Saltykov approach. The agreements between the experimental and numerical results for the fraction of graphite and the size distribution of spheroids reveal the importance of numerical models in the prediction of the main aspects of graphite in spheroidal cast iron.

I. INTRODUCTION

NODULAR cast irons are alloys in which the main components are Fe, C, and Si. From a technological perspective, the quality and mechanical properties of nodular cast irons depend on the type and characteristics of (1) graphite spheroids and (2) metallic constituents.

According to ASTM A247-10,[1] three of the main characteristics of graphite in iron castings are (1) the graphite form type (or types), (2) the graphite distribution, and (3) the graphite size class. To the best of the authors' knowledge, previous contributions have not addressed the coupling of phase transformations in liquid and solid states to monitor the evolution of these three characteristics during and at the end of the cooling process.

Studies dealing with the thermo-metallurgical evolution of the complete cooling process of spheroidal eutectic cast iron[2–6] have limited microstructural capabilities to model phase changes. During solidification, they consider a non-divorced eutectic and do not take into account mass conservation of carbon at a microstructural level. At the solid state, they do not account for microstructural characteristics at the end of solidification, such as chemical heterogeneities at the microstructural level. Moreover, in order to identify the growth stages and laws of this phase, they represent neither the growth of graphite spheroids up to the initiation of the stable eutectoid transformation, nor the bounds of the intercriticals stable and metastable eutectoid. The computation of growth rate of graphite spheroids is limited to carbon diffusion through the shell of solid solution of carbon in Fe_α (BCC iron), namely ferrite, towards the spheroids.

Venugopalan studied the growth of graphite spheroids during the continuous cooling of spheroidal cast iron.[7] The same author modeled the growth of graphite spheroids in an isothermal process.[8] In both works, there is a simplified representation of the graphite growth.

The simulation of the complete cooling of an eutectic spheroidal cast iron was presented by Wessen and Svensson.[9] In this work, the authors take into account the growth of spheroids from the end of solidification to the beginning of the stable eutectoid transformation by means of CALPHAD®.

FERNANDO D. CARAZO, Professor and Researcher, is with the Instituto de Mecánica Aplicada, Universidad Nacional de San Juan, Av. Libertador Gral. San Martín 1109 (Oeste), C.P. J5400ARL, San Juan, Argentina, and also with CONICET, C1425FQB Godoy Cruz 2290, CABA Argentina. Contact e-mail: fcarazo@unsj.edu.ar PATRICIA M. DARDATI, Professor, is with GIDMA and Departamento de Ingeniería Mecánica, Universidad Tecnológica Nacional Facultad Regional Córdoba, Maestro M. López esq. Cruz Roja Argentina s/n, Ciudad Universitaria, Córdoba, Argentina. DIEGO J. CELENTANO, Professor, is with the Departamento de Ingeniería Mecánica y Metalúrgica, Research Center for Nanotechnology and Advanced Materials (CIEN-UC), Pontificia Universidad Católica de Chile, Av. Vicuña Mackenna 4860, Macul, Santiago, Chile. LUIS A. GODOY, Professor and Researcher, is with the Institute for Advanced Studies in Engineering and Technology, FCEFyN, National University of Cordoba and CONICET, Av. Vélez Sarsfield 1601, Córdoba, Argentina, and also with CONICET.
Manuscript submitted June 9, 2015.

Lacaze and Gerval modeled the growth of graphite spheroids from the end of solidification up to environmental temperature.[10] The authors considered that up to the stable eutectoid transformation, the spheroids grow to the expense of carbon diffusion from austenite at the interphase with graphite to graphite.

Notice that Venugopalan[8] and Lacaze and Gerval[10] are the only two works in which the growth of graphite spheroids, from the end of solidification to the start of stable eutectoid phase change, has been taken into account. However, they do not couple these stages of graphite growth with microstructural solidification models. This is a severe limitation because in any cast alloy the phase changes in the solid state depend on the microstructural characteristics at the end of the solidification.

This short literature review attempts to highlight some aspects of the current state of the art:

- Conservation of carbon mass at a microstructural level has not been included in existing models. This is a crucial aspect to evaluate carbon gradient and consequently diffusion towards both spheroids and austenite located far from the interphase with graphite.
- Growth of spheroids in contact with liquid has not been considered for equiaxial dendritic morphologies which are typical in austenite for any spheroidal cast iron compositions. Furthermore, microsegregations in the liquid state and their effect on the thermodynamics and kinetics of the solid-state phase transformations are not currently modeled. These limitations do not allow investigations of how solidification processes affect graphite growth in the solid state.
- Finally, in order to distinguish the growth laws of spheroids during the stable eutectoid phase change, current models account for neither the carbon diffusion from austenite at the interphase with graphite towards the graphite spheroids, nor the intercritical stable eutectoid. For temperatures lower than the lower bound of the intercritical stable eutectoid, the present models only represent the carbon diffusion towards the spheroids through the ferrite envelope.

This paper presents a new model for nucleation and growth of graphite spheroids in an eutectic cast iron. The model aims to

- model growth of spheroidal graphite spheroids from the end of solidification to the end of austenite transformation (solid solution of C in Fe_γ or FCC iron),
- couple the growth of graphite spheroids in solid state with a microstructural model of solidification (including nucleation and growth of graphite spheroids during solidification), and
- provide a phenomenological description of the growth process of graphite spheroids in solid state, together with its implications for austenite transformations.

The model has been implemented in a computational environment where the results of the thermo-metallurgical simulations of cooling of an eutectic spheroidal cast iron are compared with results obtained in laboratory.

II. METHODOLOGY FOR THE THERMO-METALLURGICAL PROBLEM

The thermo-metallurgical cooling model developed in this research is based on two different but related scales. At a macrostructural level, the equation of energy conservation is solved to obtain the temperature (T) and cooling rate ($\dot{T}$) fields. These variables are subsequently employed as data at the microscale model, in which phase changes during solidification and in the solid state are formulated and solved at a representative volume element (RVE).[11,12] The main assumptions adopted along the cooling process are as follows: (1) the temperature is constant at each time step and its value is given from the macroscale problem solution; (2) the carbon mass conservation is satisfied; and (3) there is equilibrium at the interphases.

With T and Fe-C-Si and Fe-Fe$_3$C-Si systems (see Appendix A), it is possible to obtain the gradients of carbon concentration at different interphases, the variables required to evaluate the growth rate of phases and microconstituents, their volume fractions, and the energy released due to the latent heat during the phase changes. This energy released is part of the macrostructural formulation for the solution of the energy equation.

The macrostructural problem is solved by a finite element discretization.[13] The microstructural problems of phase changes are developed as phenomenological theories based on thermodynamics and physical metallurgy. Their results are taken to the macrostructural level in terms of rule of mixtures,[14] written as a function of the volume fraction of microconstituents and their respective latent heat values.

In Carazo et al.,[15] there may be seen a scheme of the relation between the thermal and microstructural fields in a phase-change problem solved by the finite element method, whereas the coupling scheme of the thermo-metallurgical problem is written in terms of the rate of the element phase-change vector:

$$\dot{L}_{PC}^{(e)} = \int_{\Omega_e} N^T \rho L \dot{f}_{PC} d\Omega, \qquad [1]$$

where N^T is the transpose of the shape function matrix, ρ is the density, L is the phase-change latent heat, Ω_e is the integration domain (corresponding to a finite element), and $\dot{f}_{PC}$ is the time derivative of the phase-change function which is obtained from ad hoc phase transformation models. In the macroscopic metallurgical phase-change models, f_{PC} is an explicit function of T. On the contrary, in the metallurgical phase-change models defined from a microstructural

standpoint, f_{PC} is written in terms of T and a set of microstructural state variables.

The phase changes considered in this work are defined from microstructural models. Assuming that a local state field is the mean volumetric value in a statistically representative microstructural domain of the material simple at the macroscopic level (RVE), in this work, the rate of the element phase-change vector can be expressed as

$$\dot{L}_{PC}^{(e)} = \int\limits_{\Omega_e} N^T \rho L \frac{\partial(A_{\alpha m_i} \alpha_{m_i})}{\partial T} \dot{T} d\Omega,$$

where $A_{\alpha_{mi}}$ and α_{mi} are the set of state variables and the corresponding parameters of the phase-change models (e.g., solidification and transformations in solid state). Thus, the phase-change effects described at the microscopic level can be taken into account at the macroscopic level in the energy balance as a variable source term.[13]

III. SOLIDIFICATION OF EUTECTIC SPHEROIDAL CAST IRON

A. *Phenomenological Approach at the Microstructural Level*

In spheroidal cast irons, the eutectic transformation develops according to a divorced eutectic, also known as anomalous.[16,17] This is a difference with flake cast irons in which the eutectic transformation occurs as a regular eutectic which is characteristic of a faceted–faceted morphology, *i.e.*, flake graphite–austenite.

In spheroidal cast irons, eutectic crystallization is produced from the independent nucleation of graphite spheroids and equiaxed austenite dendrites at different points, undercooling, and time stages.[18–22] There have been observations showing that graphite spheroids nucleate around austenite dendrites and vice versa in some cases. This does not seem to be a direct phenomenon but rather it is due to the gradient of C composition which produces primary nucleation and growth of austenite and graphite.[21]

The microstructure of spheroidal cast irons at the end of the solidification, which shows graphite spheroids in an austenite matrix, is characterized by a divorced eutectic according to the theory of solidification.[23,24] This is justified because in a divorced eutectic, once the faceted face (which is spheroidal graphite in this case with high fusion entropy) nucleates, it requires a large undercooling to grow with respect to the non-faceted phase (austenite). The non-faceted phase nucleates and grows according to the metastable extrapolation of the liquidus line. This occurs until the formation and growth of the faceted phase becomes favored at a higher undercooling. At this stage, the growth of both phases occurs in the zone of the metastable extrapolation of the equilibrium Fe-C-Si system at temperatures lower than eutectic temperatures.

Due to the carbon enrichment of the remaining liquid in areas around equiaxed austenite dendrites that have nucleated, this path of solidification enters the zone of coexistence or coupled growth (austenite–graphite),

which is shifted to the zone of the faceted phase because, as mentioned above, it is the phase with higher fusion entropy.[25]

Following the description provided above in this section, the microstructure of a spheroidal cast iron is formed by a divorced eutectic and, depending on the characteristics of the solidification process, may (or may not) show eutectic cells as have been reported from various experiments.

B. *Microstructural Model*

Most metallurgical research at micro level dealing with solidification of spheroidal cast irons considers a non-divorced eutectic with cooperative growth. The underlying assumption is that the spheroids that nucleate are instantly surrounded by austenite.[2–4,18,20,25–43] However, according to the process described in Section III–A, the thermodynamics and kinetics of the eutectic transformation would not be related to a non-divorced eutectic. In agreement with this line of thought, the phase-change model should account for independent nucleation of austenite and graphite in the liquid and, in addition, independent equiaxial dendritic growth of austenite and spherical growth of graphite in the liquid and in contact with the austenite.

The main features of the microstructural model for solidification of an eutectic spheroidal cast iron adopted in this work are presented below. In this model, originally proposed by Dardati,[11] a divorced eutectic is considered. A scheme of a two-dimensional grain of austenite, together with graphite spheroids and carbon concentration profile, is shown in Figure 1.
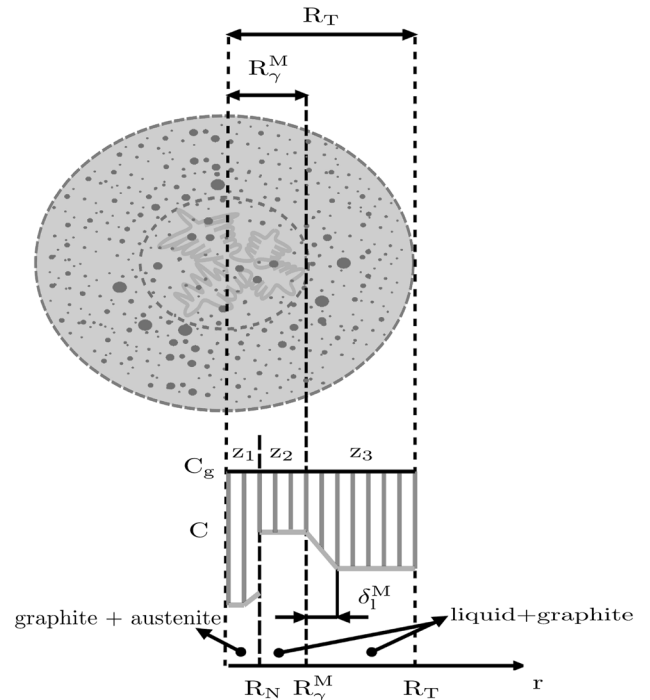

Fig. 1—Scheme of the representative volume element and the carbon distribution profile during the eutectic solidification of a spheroidal graphite cast iron.[11]

The main assumptions considered in the work of Dardati[11] are as follows: (1) instantaneous nucleation of austenite; (2) continuous nucleation of graphite; (3) equiaxial dendritic growth of austenite; (4) the growth rate of the main branches of dendrites is given by the equation of kinetics of growth of an isolated dendrite; (5) spherical growth of graphite; (6) the carbon diffusion in solid state is neglected; (7) carbon mass balance is preserved at a representative volume element; (8) uniform carbon composition in the interdendritic liquid; and (9) spherical carbon diffusion in the intergranular liquid.

The main results of the model proposed by Dardati[11] are as follows: (1) austenite and graphite volume fractions, (2) number and size distribution of graphite spheroids; (3) alloy composition of the first and last zone that become solid; and (4) grain size of austenite.

According to Figure 2, which shows a schematic part of a pseudo-binary Fe-C-Si system, the composition of the alloy considered in this study varies along the three zones z_1, z_2, and z_3 in Figure 1. The main features of the nucleation and growth models of graphite spheroids during an eutectic solidification are presented in Sections III–C and III–D. Details of such models may be found in Dardati et al.[44]

C. Nucleation of Graphite Spheroids

As mentioned above, the nucleation of graphite spheroids is modeled as a continuous process. The process starts when the alloy temperature reaches the eutectic temperature (point C' in Figure 2), it stops under recalescence and, finally, it restarts if the temperature is lower than the lowest temperature at which the process had previously stopped, before the end of solidification (z_2 and z_3 in Figure 1). In this context, nucleation is assumed to occur in the interdendritic and intergranular zones (zones z_2 and z_3, respectively).

D. Growth of Graphite Spheroids

Graphite spheroids in zone z_1 are assumed to not grow since the solidification model does not consider carbon diffusion in solid state. The graphite spheroids surrounded by interdendritic or intergranular liquid (zones z_2 and z_3 in Figure 1, respectively) continue their growth as a function of the respective carbon diffusion in those zones.

The carbon concentration profile is taken to be uniform (unlike that shown in Figure 1 which was only employed to model the growth of the austenite dendrite). Notice that although the interphases are assumed to be in equilibrium (same as in the growth model of spheroids in solid state),[12] the modeling of phase changes in which nucleation of austenite and graphite spheroids takes place allows incorporating the characteristic incubation time of phase changes out of equilibrium. In this case, the carbon concentrations are obtained by means of a procedure proposed by Heine[45] which is based, for temperatures lower than the eutectic one, on a metastable extrapolation reported by Hultgren.[46]

IV. GROWTH OF GRAPHITE SPHEROIDS FROM THE END OF SOLIDIFICATION UP TO THE UPPER BOUND OF THE INTERCRITICAL STABLE EUTECTOID

A. General Considerations

For a temperature T^* lower than the eutectic temperature ($T_{E'}$) and higher than the upper bound of the intercritical stable eutectoid ($T_{a_T}^\alpha$), the equilibrium carbon concentration in austenite at the interphase with graphite ($C_C^{\gamma/g}$) is shown in Figure 2. The carbon concentration profile for such temperature range and a quarter of a graphite spheroid surrounded by austenite are both depicted in Figure 3. If the temperature decreases, Figure 2 shows that the carbon solubility in austenite decreases along the line $E'S'$. As the cooling of the cast part progresses, for each temperature between $T_{E'}$ and $T_{a_T}^\alpha$, the values of $C_C^{\gamma/g}$ will be given by the equilibrium carbon concentrations in austenite at the
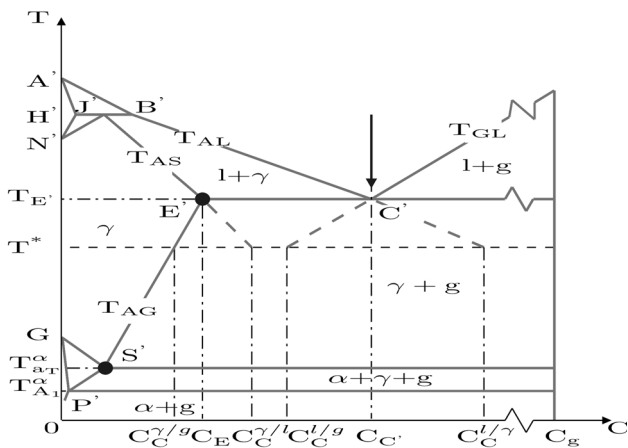

Fig. 2—Schematic of an isopleth Fe-C section of the Fe-C-Si equilibrium phase diagram with the composition of interest for a temperature $T_{a_T}^\alpha \leq T^* \leq T_{E'}$.
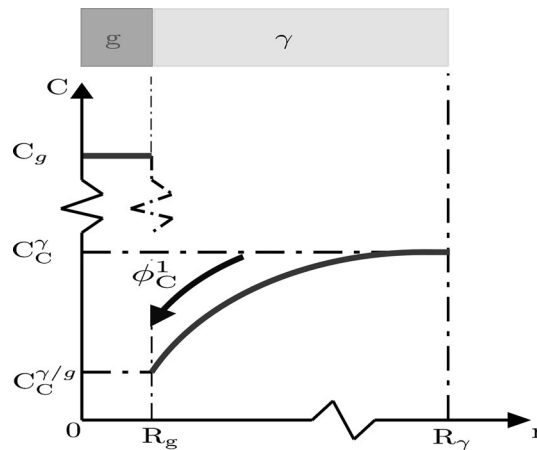

Fig. 3—Schematic representations of one quarter of a graphite spheroid surrounded by austenite and the associated carbon profile for a temperature between $T_{E'}$ and $T_{a_T}^\alpha$.

interphase with graphite in the Fe-C-Si system (see Appendix A).

B. *Growth Rate of Graphite Spheroids*

Based on the consideration made at the beginning of this section and assuming that the difference between $C_C^{\gamma/g} - C_C^\gamma < 0$, where C_C^γ is the carbon content in austenite, the flow of carbon from the austenite to the graphite spheroids, indicated as ϕ_C^1 in Figure 3, is computed by a Fick-type equation[47] in the form:

$$\phi_C^1 = -D_C^\gamma \rho_\gamma \frac{\partial C_C^\gamma}{\partial r}\bigg|_{r=R_g}, \qquad [2]$$

where D_C^γ is the diffusion coefficient of carbon in austenite, ρ_γ is the density of austenite, and $\partial C_C^\gamma/\partial r\big|_{r=R_g}$ is the gradient of carbon in austenite at the interphase with graphite. Carbon that diffuses from austenite to the graphite spheroids is incorporated into the latter as

$$\phi_C^1 = \left(\rho_g C_g - \rho_\gamma C_C^{\gamma/g}\right) \dot{R}_g, \qquad [3]$$

where C_g and ρ_g are the carbon concentration and density of graphite, respectively, and $\dot{R}_g$ is the rate of change of graphite spheroids radius (*i.e.*, the rate at which the graphite/austenite interphase advances towards austenite). From Eqs. [2] and [3], it results

$$\dot{R}_g = D_C^\gamma \rho_\gamma \frac{1}{\left(\rho_g C_g - \rho_\gamma C_C^{\gamma/g}\right)} \frac{\partial C_C^\gamma}{\partial r}\bigg|_{r=R_g} \qquad [4]$$

where $\partial C_C^\gamma/\partial r\big|_{r=R_g}$ is the only unknown in the right-hand side of Eq. [4] whose evaluation requires knowledge of the profile shape of carbon through the austenite. Considering that the rate of carbon diffusion from the austenite to the graphite spheroids is higher than the rate of advance of the spheroids towards austenite, it is possible to assume that carbon diffusion is a quasi-stationary process. Thus, according to Shewmon,[48] the gradient of C_C^γ for a quasi-stationary solute profile with the boundary conditions on the spheroid shown in Figure 3 is

$$\frac{\partial C_C^\gamma}{\partial r}\bigg|_{r=R_g} = \frac{\left(C_C^\gamma - C_C^{\gamma/g}\right)}{R_g}. \qquad [5]$$

Substituting Eq. [5] into Eq. [4], the radius rate of graphite spheroids from the end of solidification until the upper bound of intercritical stable eutectoid is given by

$$\dot{R}_g = \frac{D_C^\gamma}{R_g} \frac{\left(C_C^\gamma - C_C^{\gamma/g}\right)}{\left(\rho_g/\rho_\gamma C_g - C_C^{\gamma/g}\right)}. \qquad [6]$$

The growth of spheroids occurs at the expense of carbon diffusion from the austenite, so that the carbon content in the austenite decreases in accordance with an increase in size of the spheroids. Thus, C_C^γ must be computed whenever there is a change in the size of the spheroids taking into account that its initial value is obtained from that at the end of the solidification. Spheroids stop their growth when $C_C^{\gamma/g} - C_C^\gamma > 0$.

V. GROWTH OF GRAPHITE SPHEROIDS DURING THE STABLE EUTECTOID PHASE CHANGE

The growth of graphite spheroids during the stable eutectoid phase change can be considered in two steps that are separately described below.

A. *Growth of Graphite Spheroids During the Intercritical Stable Eutectoid*

Figure 4 shows a schematic Fe-C section of the Fe-C-Si equilibrium phase diagram for a temperature between the upper and lower bounds of the intercritical stable eutectoid.

When the temperature is between the upper and lower bounds of the intercritical stable eutectoid ($T_{a_T}^\alpha$ and $T_{A_1}^\alpha$, respectively), the growth of graphite spheroids is due to the carbon diffusion caused by the difference between the values of C_C^γ and $C_C^{\gamma/g}$, as long as $C_C^{\gamma/g} - C_C^\gamma < 0$ (see Figure 3). If the temperature reaches $T_{a_T}^\alpha$, the ferrite grains can nucleate on the surface of the spheroids in such a way that the graphite is covered by ferrite grains depending on its size and on the number and size of ferrite nuclei that nucleate on the surface of each spheroid.

Unlike what was discussed in Section IV, carbon diffusion could take place now through ferrite and austenite. The growth rate of graphite spheroids in the intercritical stable eutectoid is computed by considering that the equilibrium carbon concentration in ferrite in
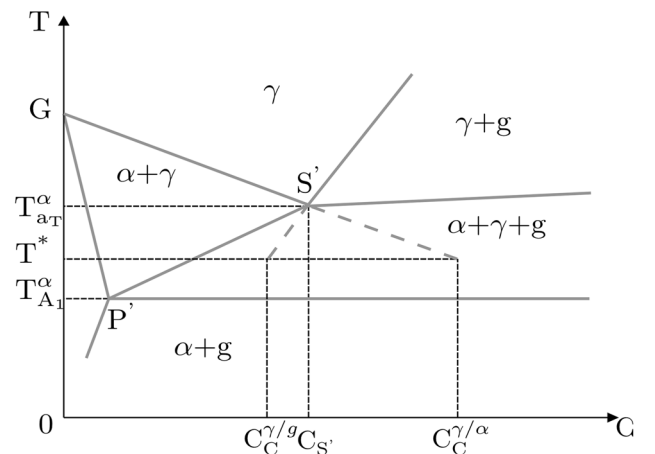

Fig. 4—Schematic of an isopleth Fe-C section of the Fe-C-Si equilibrium phase diagram with the indication of stable and metastable equilibrium carbon concentrations (solid and broken lines, respectively) for a temperature between the upper and lower bounds of the intercritical stable eutectoid.
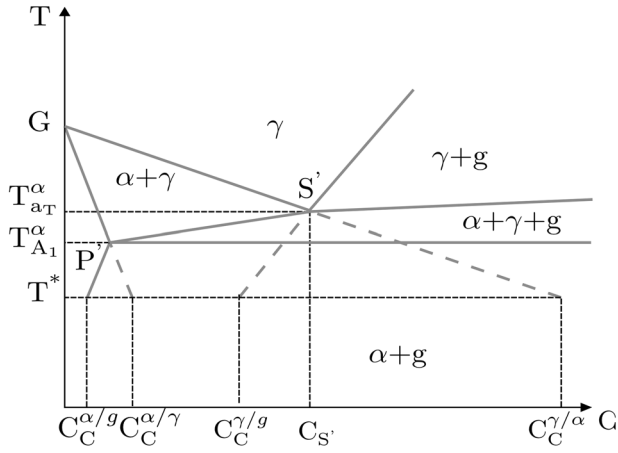
Fig. 5—Schematic of an isopleth Fe-C section of the Fe-C-Si equilibrium phase diagram with the indication of stable and metastable equilibrium carbon concentrations (solid and broken lines, respectively) for a temperature lower than the lower bound of the intercritical stable eutectoid.
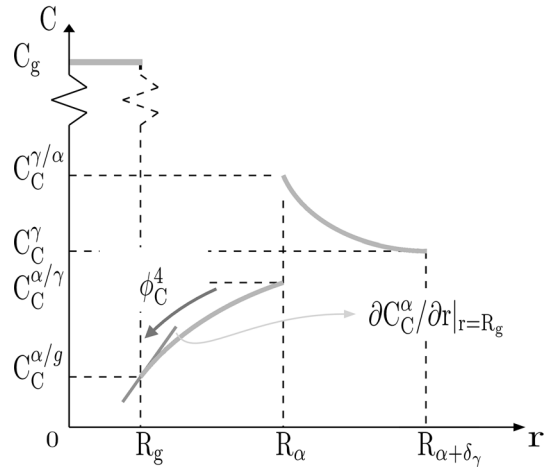

Fig. 6—Indication of the carbon gradient that gives rise to ϕ_C^4 and the carbon distribution during graphite growth for a temperature lower than the lower bound of the intercritical stable eutectoid (see Fig. 5).

contact with austenite ($C_C^{\alpha/\gamma}$) is lower than the equilibrium carbon concentration in ferrite in contact with graphite ($C_C^{\alpha/g}$). This may be seen in Figure 5 which shows a schematic Fe-C section of the Fe-C-Si equilibrium phase diagram for a temperature lower than the lower bound of the intercritical stable eutectoid, by extrapolation of the line of $C_C^{\alpha/g}$ at temperatures higher than the lower bound of the intercritical stable eutectoid.

Thus, the radius rate of graphite spheroids is given by

$$\dot{R}_g = \frac{D_C^\gamma}{R_g} \frac{\left(C_C^\gamma - C_C^{\gamma/g}\right)}{\left(\rho_g/\rho_\gamma C_g - C_C^{\gamma/g}\right)} A_{\gamma/g} \qquad [7]$$

where the coefficient $A_{\gamma/g}$ takes into account the fraction of the spheroid surface in contact with austenite, i.e., $0 \leq A_{\gamma/g} \leq 1$, such that $A_{\gamma/g} = 1$ for the start of the transformation, while $A_{\gamma/g} = 0$ is achieved when the spheroid is completely covered by ferrite grains, and $A_{\gamma/g}$ is calculated as proposed in Appendix B. In Eq. [7], a spheroid that is fully covered by ferrite ($A_{\gamma/g} = 0$) means that it is not in contact with austenite and this implies that there is no carbon diffusion from such phase to the graphite spheroids. The value of $C_C^{\gamma/g}$ in Eq. [7] is obtained by extrapolation of the line of maximum solubility of carbon in austenite for temperatures lower than $T_{a_T}^\alpha$, depending on the values of silicon concentration in austenite in contact with graphite C_{Si} or in the first zone of solidification (see Appendix A). The carbon profile considered in this growth step is shown in Figure 6.

B. Growth of Graphite Spheroids at Temperatures Lower than the Lower Bound of the Intercritical Stable Eutectoid

As the ferrite grains have nucleated on the spheroids, when the temperature is lower than the lower bound of the intercritical stable eutectoid (see Figure 5), the spheroids grow as a function of carbon diffusion to the graphite through ferrite if $A_{\gamma/g} = 0$ (flow ϕ_C^4 in Figure 6) and through ferrite and austenite if $A_{\gamma/g} \neq 0$ (flows ϕ_C^4 and ϕ_C^1 shown in Figures 3 and 6, respectively).

1. Growth rate of graphite spheroids completely covered by ferrite

In a graphite spheroid that has been completely covered by ferrite grains that nucleated on its surface, the flow of carbon allowing for the growth of graphite spheroids is given by

$$\phi_C^4 = -D_C^\alpha \rho_\alpha \frac{\partial C_C^\alpha}{\partial r}\bigg|_{r=R_g}, \qquad [8]$$

where ρ_α is the density of ferrite, D_C^α is the diffusion coefficient of carbon in ferrite, and $\partial C_C^\alpha/\partial r\big|_{r=R_g}$ is the gradient of carbon concentration in ferrite in contact with graphite (straight line at $r = R_g$ in Figure 6).

Under the same assumptions of Section IV–B, in this case the gradient of Eq. [8] depends on $C_C^{\alpha/g}$ and $C_C^{\alpha/\gamma}$ (see Figure 6) and, therefore, the growth rate of the graphite spheroid radius results in

$$\dot{R}_g = D_C^\alpha \frac{\rho_\gamma}{\rho_\alpha} \frac{\left(C_C^{\alpha/\gamma} - C_C^{\alpha/g}\right)}{\left(C_g - C_C^{\alpha/g}\right)} \frac{R_\alpha}{R_g(R_\alpha - R_g)}. \qquad [9]$$

2. Growth rate of graphite spheroids partially covered by ferrite grains

If a graphite spheroid has not been completely covered by ferrite grains that nucleated on its surface, the flow of carbon to the spheroid occurs through ferrite and austenite. In this case, the growth rate of the graphite spheroid radius may be written as

$$\dot{R}_g = \dot{R}_g\big|_\gamma A_{\gamma/g} + \dot{R}_g\big|_\alpha A_{\alpha/g}, \qquad [10]$$

where $A_{\alpha/g}$ is the fraction of the spheroid surface in contact with ferrite which is calculated as proposed in Appendix C. The growth rates of the right-hand side of Eq. [10] are computed from Eqs. [6] and [9], respectively.

From the value of the radius of the graphite spheroids (Eqs. [6], [7], [9], [10]), it is possible to calculate the volume fraction of graphite as shown in Appendix C and, then, the value of C_C^γ according to Appendix D.

VI. EXPERIMENTAL AND COMPUTATIONAL PROCEDURES

A. Experiments

The alloy employed in the tests was molten in a high-frequency induction furnace with 1500 kg capacity. Its composition was approximately 23.3 pct of SAE 1010 scraps, 23.3 pct of retrieved nodular cast iron, 6.6 pct of pig iron, and 41.8 pct of charcoal. To obtain the adequate carbon content, 1.6 pct of carbon (with a 90 pct of performance), 2 pct of steel plates, and 0.15 pct of SiCa and thick Fe-Si (with 75 pct of Si) were added to adjust the Si composition of the base metal in the molten furnace. The base metal was overheated to 1923 K (1650 °C) during approximately 20 minutes where 1.5 pct Fe-Si-Mg-Ce was used as a nodularizing agent.

Inoculation and nodularization were done by the sandwich method. In the reaction ladle, 0.7 pct of fine FeSi (with 75 pct of Si) was added. The cast metal was poured into the cast ladle to fill the cups shown in Figures 7(a) and (b). Five cups typically used to determine the carbon equivalent were also employed in this study. Table I shows the main components of the alloy used in the experiments (in weight percentage).

The thermal history was recorded by means of cooling and cooling rate curves at the central zone of the part (zone 5 in Figure 7(c)). The metallurgical study encompasses the characterization of the graphite spheroids and the determination of graphite, ferrite, and pearlite phase fractions in five zones of Figure 7(c).

To characterize the graphite spheroids, the cast parts were divided in two parts following a longitudinal plane. Each half specimen (see Figure 7(c)) was roughed by conventional procedures, subsequently polished with alumina, and, finally, observed using an optical microscope.

In order to identify and characterize the graphite spheroids, the micrographs ($\times 100$) corresponding to the five zones shown in Figure 7(c) were analyzed and processed using the software ImageJ.[49,50] Three important aspects were considered during these stages:

1. The results obtained were limited to objects for which the aspect ratio was larger than 0.9.
2. The minimum diameter to consider an object as a graphite spheroid was defined as 6 μm.
3. The size of each pixel was 0.3478 μm.

For the five zones shown in Figure 7(c), the following procedure was considered:

1. Micrographs without chemical etching were used to analyze and characterize graphite spheroids.
2. Micrographs with chemical etching were used to quantify the microconstituents corresponding to the metal matrix.

The characterization of the graphite spheroids included the following:

1. Quantification of the graphite fraction per unit area.
2. Measurement of the area of each object. This allowed estimating the diameter of each sphere as equivalent to the identified object by application of the criterion to determine the equivalent diameter of a sphere of the same projected area.

Table I. Average Chemical Composition (Main Elements) of the Molten Alloy (Values in Wt. Pct)

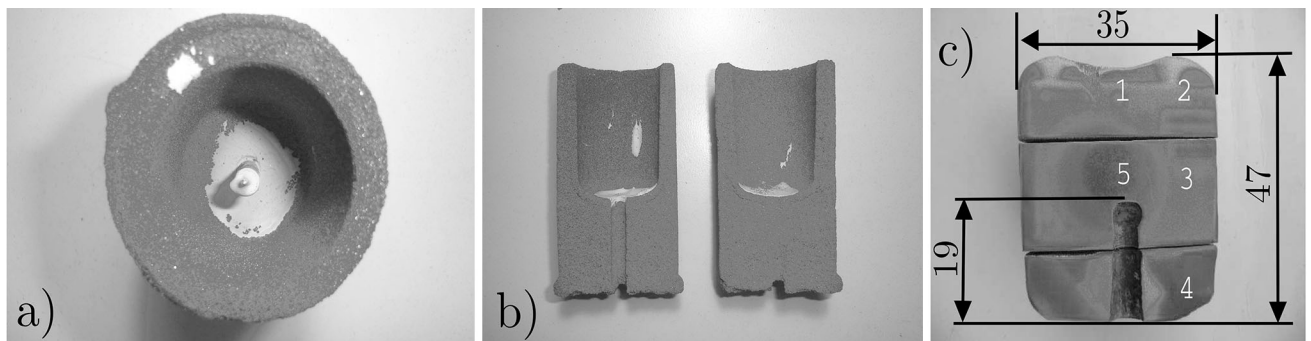| Element	C	Si	Mn	S	P	Cr	Cu	Sn	Mg	CE
Wt. Pct	3.67	2.8	0.21	0.01	0.038	0.025	0.01	0.0009	0.052	4.61

Fig. 7—Cylindrical cup used to determine carbon equivalent and specimen poured used in the laboratory experiments. (a) Top view in which the bifilar ceramic and the thermocouple covered by refractory cement can be observed. (b) Longitudinal midplane section view. (c) Longitudinal midplane section view of the specimen with its dimensions (in mm) and the indication of five microstructurally characterized zones.

With the diameter of the identified objects (obtained with ImageJ in each micrography), it was possible to obtain

1. Number of spheroids per unit volume as a function of their sizes,
2. Distribution of graphite fractions in terms of the spheroid sizes,
3. Distribution of the accumulated graphite fraction in terms of the spheroid sizes, and
4. Volume graphite fraction.

All the values mentioned were obtained from the size distribution of spheroids per unit area and volume (with the exception of the graphite fraction, which only is obtained from the size distribution of spheroids per unit volume).

A brief description of the methodology used to obtain the number of spheroids per unit volume as a function of their sizes is presented below.

For each micrography, once the largest diameter of an object (d_{max}) was identified and the desired number of classes to investigate the size distribution was selected ($n_{classes}$), the interval Δ between one diameter d_{i-1} and the next d_i is $\Delta = {d_{max}}/{n_{classes}}$, obtaining Table II.

Known Δ, the diameter of spheroids, the number of classes, and the area of the micrographs, the size distribution of spheroids per unit area of the corresponding micrography area was calculated ($N_{gr_{A_i}}$). This allowed the calculation of the number of graphite spheroids per unit volume ($N_{gr_{V_i}}$) according to Schwartz–Saltykov approach.[51]

Next, the distributions of graphite fractions (per unit area $f_{gr_{A_i}}$ and volume $f_{gr_{V_i}}$) were obtained allowing, finally, the evaluation of the accumulated graphite fractions per unit area ($f_{gr_A} = \sum_{i=1}^{n_{classes}} f_{gr_{A_i}}$) and volume ($f_{gr_V} = \sum_{i=1}^{n_{classes}} f_{gr_{V_i}}$). A statistical analysis, aimed at increasing the representativity and reliability of the measurements, was performed in order to obtain a single value at the central zone of the each cast part (zone 5 in Figure 7(c)) since it was the only zone for which the cooling curve was measured.
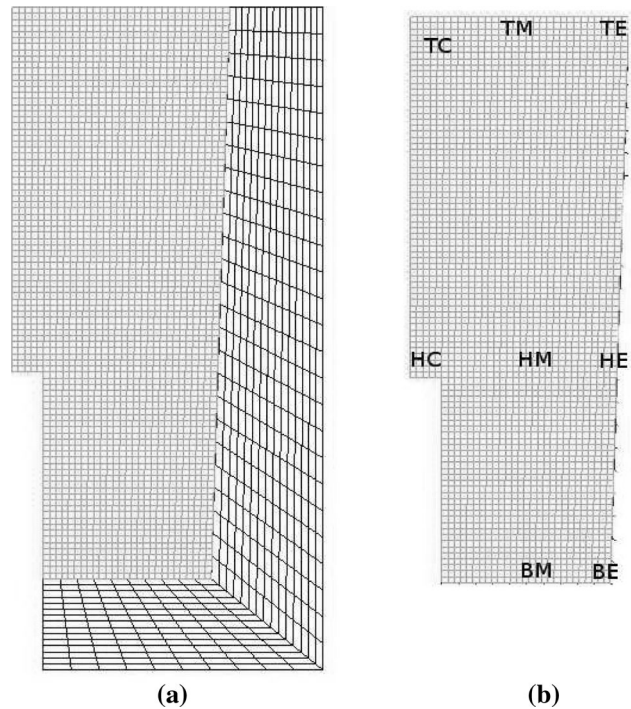
B. Computational Procedure

Due to axial symmetry of the part employed in the cast (see Figures 7(a) and (b)), only a half of the longitudinal plane was discretized with quadrilateral four-noded elements where 2838 and 525 were used to represent the cast part and the mold, respectively; see Figures 8(a) and (b). Contact elements were used to simulate the heat flow between the part and the cup, whereas surface elements were considered to deal with the heat extraction through convection in the external surface of the part and the mold in contact with the ambient temperature.

All the thermo-physical properties and material parameters used in the numerical simulations are given in Appendix E.

VII. RESULTS AND DISCUSSION

A. Numerical Results

Numerical cooling and cooling rate curves computed at the nodes indicated in Figure 8(b) are, respectively, plotted in Figures 9 and 10. Both plots also show an enlargement of the areas of interest. Table III summarizes the solidification time values. From Figure 9, there is a relation between the local time of solidification (t_f) indicated in Table III and the plateau of the characteristic region of solidification. From the end of

Table II. Graphite Spheroid Diameters Delimiting Each Class

	Diameter (m) $\times 10^{-6}$	
Class	Smaller	Larger
1	6	10.72
2	10.72	15.44
3	15.44	20.16
4	20.16	24.88
5	24.88	29.6
6	29.6	34.32
7	34.32	39.04
8	39.04	43.76
9	43.76	48.48
10	48.48	53.2
11	53.2	57.92
12	57.92	62.64
13	62.,64	67.36
14	67.36	72.08
15	72.08	76.8

Fig. 8—FE mesh used in the simulations. (*a*) Axisymmetric FE mesh of the specimen and mold. (*b*) Location of the nodes where the results are analyzed.

solidification and up to the beginning of the stable eutectoid transformation, the curves do not exhibit any special feature of interest. During the eutectoid transformations, the segment of the cooling curves have a direct relation with the initiation time of the stable eutectoid transformation listed in Table III (t_α^{ini}). The first nodes starting the stable eutectoid phase change are those having the highest cooling rate at the beginning of its transformation (see Table III and Figure 10). During the solidification as well as during the stable and metastable eutectoid transformations, the nodes that show the highest recalescence values in both cases are those placed in the central region of the specimen (*i.e.*, nodes identified as HC, HM, and HE) which is, in fact, the hot spot as the cooling process progresses. Therefore, the cooling rate (see Figure 10), and consequently the latent heat released during the phase changes, becomes slower in the central zone of the casting.

The above thermal consideration is relevant because of the influence of temperature on diffusive phase changes. The driving force for nucleation increases with over-cooling, which increases with the thermal cooling rate, and stops at recalescence. The growth rate of spheroids increases with atomic mobility, *i.e.*, higher temperatures (we consider the influence of Si on the thermodynamics of phase changes only, not in its

kinetics). Plots of the graphite fraction evolution at the nodes shown in Figure 8(b) are shown in Figure 11.

Processes of nucleation and growth of graphite spheroids are indicated following the three steps identified in this paper (Sections III–D, IV, and V): solidification, from the end of solidification up to the beginning of the stable eutectoid transformation, and, finally, eutectoid transformations.

In the first step, the growth rate of the graphite fraction has a direct relation with cooling rate of the corresponding nodes (see Figure 10 and Table III). This seems to be justified because a higher cooling rate increases the undercooling and, thus, the driving force for graphite nucleation. The evacuation of the energy released during the phase change (due to both latent heats of solidification of graphite and austenite) is higher in regions of the part with higher cooling rate, with the consequence that the criterion established to end the nucleation (presence of recalescence) is less likely to occur in these regions than in the others with lower cooling rate. The plateau which is observed at the

Table III. Solidification Time (t_f), Initiation Time of the Stable Eutectoid Transformation (t_α^{ini}), and Cooling Rate Before Solidification Start ($\dot{T}$)

Node	t_f (s)	t_α^{ini} (s)	$\dot{T}$ (K/s)
TE	124	442	−2.6
TM	130	448	−2.5
TC	144	450	−2.47
BE	148	456	−2.92
BM	152	460	−2.66
HE	176	464	−2.2
HM	180	466	−1.76
HC	180	468	−1.72

Fig. 10—Cooling rate curves with magnification of solidification and eutectoid zones.
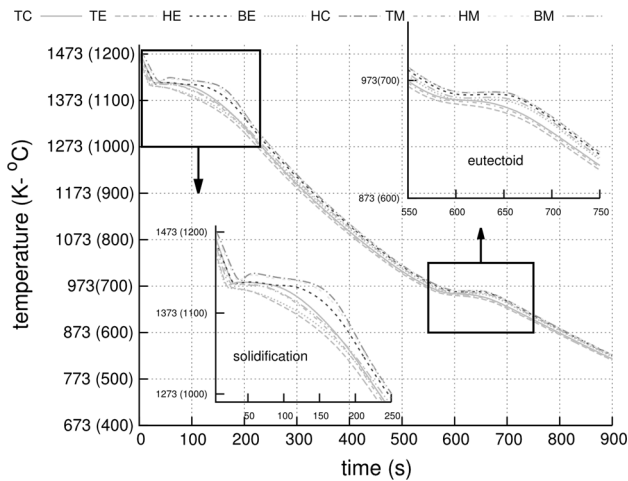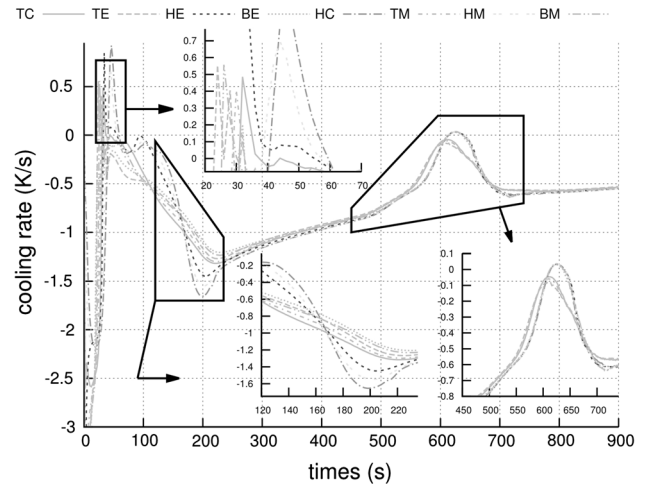

Fig. 9—Cooling curves with magnification of solidification and eutectoid zones.
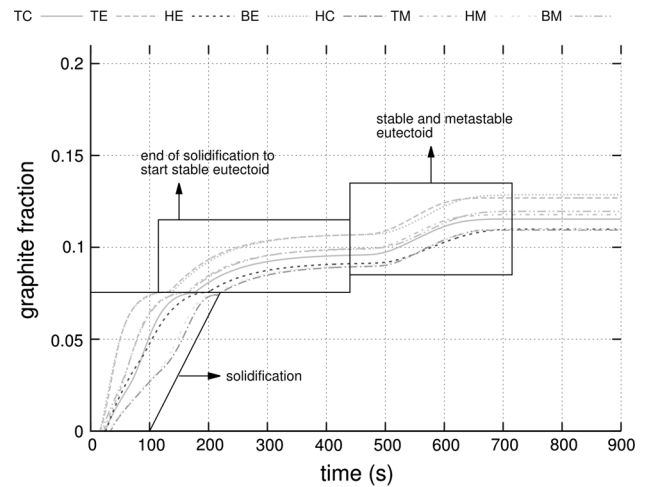

Fig. 11—Graphite fraction evolution.

end of this step occurs because the microstructural model of solidification considers that the spheroids stop their growth if they are not in contact with liquid (zone 1 in Figure 1). This seems reasonable on account of the soft and hard impingement that takes place towards the end of any diffusive phase change.

During the second step, the spheroids grow by carbon that leaves the austenite (line $\overset{.}{E}\overset{.}{S}$ in Figure 2). The growth rate of spheroids at the initiation of this second stage is lower than that of solidification, because this is a solid-state diffusive process in which the atomic mobility is lower than that in a liquid state, and decreases with decreasing temperature and value of the diffusion coefficient of carbon in austenite.

Finally, during the stable and metastable eutectoid phase changes in the third step, the growth rate of the graphite spheroids increases with respect to that at the end of the second step and, as already discussed in Section V, takes place in two parts.

The graphite fraction, its trend in terms of the cooling rate at the initial instants of solidification, and its mean value (see Table III) for the nodes indicated in Figure 8(b) are shown in Figure 12.

The trend (a straight line obtained by a least square approximation) shows that by increasing cooling rates the graphite fraction also increases. The value of the correlation coefficient (−0.87) highlights this fact. The horizontal line, on the other hand, is associated with the mean graphite fraction value of 11.73 pct.

Figure 13 shows percentage of the final graphite fraction in terms of the cooling rate transformed at the final instants of solidification, from the end of solidification up to the start of stable eutectoid phase change, and during the stable and metastable eutectoid phase changes.

As the cooling rate decreases during solidification, the graphite fraction increases. However, from the end of solidification up to the upper bound of intercritical stable eutectoid, an increasing trend is predicted. From a phenomenological point of view, this could be due to the lower carbon quantities in austenite as the carbon quantity in the form of graphite phase increases. For the stable and metastable eutectoid transformations, as expected, correlation is the lowest out of the three stages taken into account in this plot (0.77, as compared with −0.88 and 0.85) because the most influential variables for graphite growth in this transformation are not directly related with the cooling rate at the start of solidification.

Plots of the percentage of the total graphite fraction that has been transformed between the end of solidification and the start of the stable eutectoid phase change in terms of the elapsed time for this stage are presented in Figure 14, together with the trend line and associated mean value as a function of time.

It is seen that there is a direct relation between the final graphite fraction that has been transformed during this stage and elapsed time of this stage. The mean value
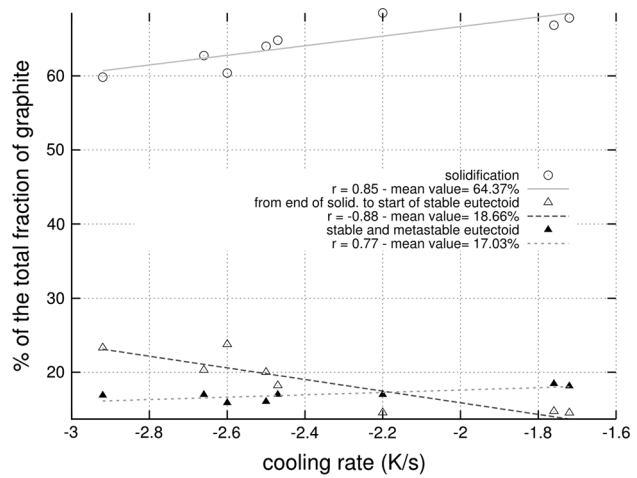

Fig. 13—Percentage of the final graphite fraction as a function of the cooling rate transformed at the final instants of the three stages of graphite growth for the nodes shown in Fig. 8(b).
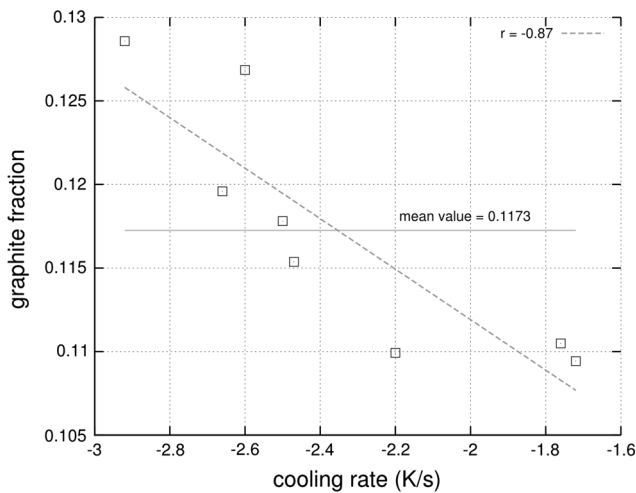

Fig. 12—Graphite fraction as a function of the cooling rate at the initial instants of solidification for the nodes shown in Fig. 8(b).
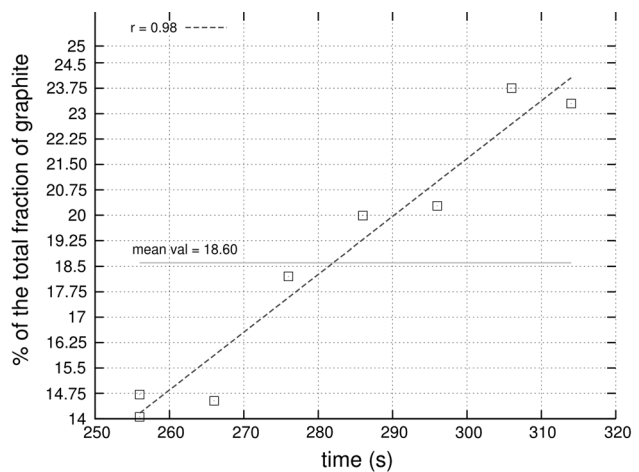

Fig. 14—Percentage of the final graphite fraction transformed from the end of solidification up to the start of the stable eutectoid transformation as a function of the elapsed time for this stage for the nodes shown in Fig. 8(b).
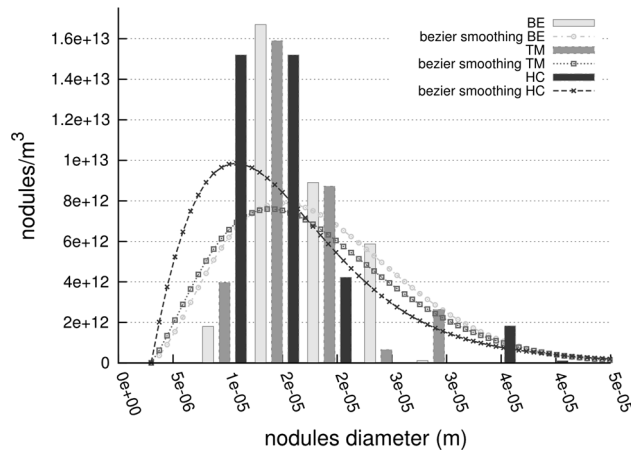
Fig. 15—Discrete and continuous quantities of graphite spheroids per unit volume as a function of their sizes for nodes BE, TM, and HC (according to the classes listed in Table II).

is 18.6 pct of the final fraction, which is very close to the value of 19 pct indicated in Figure 13.

Discrete and continuous distributions of graphite spheroid quantities as a function of their size (as specified in Table II) are shown in Figure 15 for nodes BE, TM, and HC identified in Figure 8(b), which are those exhibiting, as shown in Table III, the highest, mean, and the lowest cooling rates, respectively.

There is a similar distribution for the three nodes, with a tendency of peaks to shift towards larger diameters when cooling rate, at the start of solidification, increases, and consequently graphite volumetric fraction also increases. The peak of the continuous distribution tends to be higher and to shift towards smaller diameters as the cooling rate at the start of solidification is lower. The shift of the peak in the continuous distribution to larger diameters (higher classes in Table II) and values of graphite volumetric fraction at nodes BE, TM, and HC (see Figure 11) evidence that graphite volumetric fraction tends to increase as the distribution of numbers of spheroids shifts towards the higher classes.

B. Comparison Between Numerical and Experimental Results

Computed cooling curves and cooling rate curves at the central region of the sample are, respectively, compared in Figures 16 and 17 with those corresponding to three experiments.

The complete curve in Figure 16 shows good agreement between experiments and computations. As shown in Figure 17, there is also a good prediction of the local and global solidification times, evidenced at the characteristic zones in Figure 17. Regarding the stable and metastable eutectoid phase changes, the small change in slope in the numerical cooling rate curves shows that the stable eutectoid transformation starts at 468 seconds. Although there are differences between cooling curves in the eutectoid region, the starting time of the stable eutectoid phase change in the simulation is close to that of
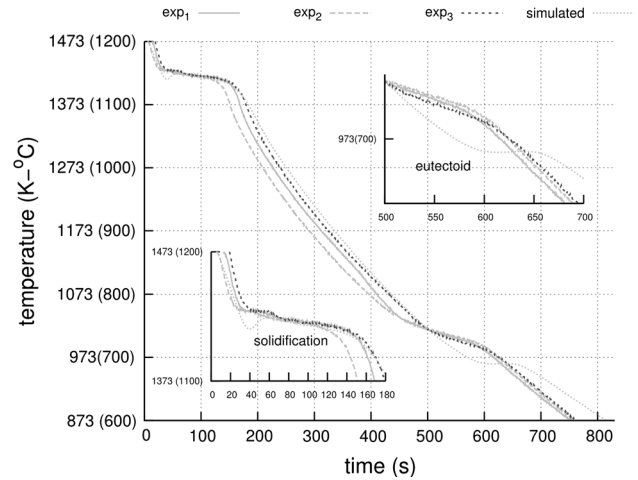

Fig. 16—Comparison of simulated and experimental cooling curves at the central zone of the specimen with magnification of solidification and eutectoid zones (zone 5 in Fig. 7(c) and node HC in Fig. 8(b)).
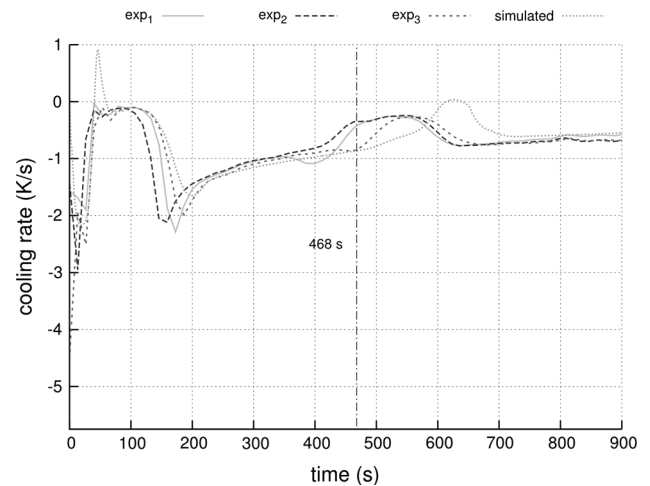

Fig. 17—Comparison of simulated and experimental cooling rate curves at the central zone of the specimen (zone 5 in Fig. 7(c) and node HC in Fig. 8(b)).

the experiments. This could suggest an underestimate of the latent heat of the stable eutectoid phase change.

Discrete numbers of spheroids per unit area and volume, as obtained from experiments and simulation at zone 5 in Figure 7(c) and node HC in Figure 8(b), are illustrated in Figure 18 following the definition of classes and diameters listed in Table II. The three discrete distributions and their interpolated continuous forms in Figure 19 show similar trends, but the peak in the simulation is shifted towards classes with larger diameters.

Figure 20 shows discrete distributions of graphite fractions from experiments and simulations at the central region, whereas continuous distributions are plotted in Figure 21. The experiments show three peaks, while the simulations show only two. The peak in the experiments associated with large diameters occurs because of primary spheroids (a hypereutectic
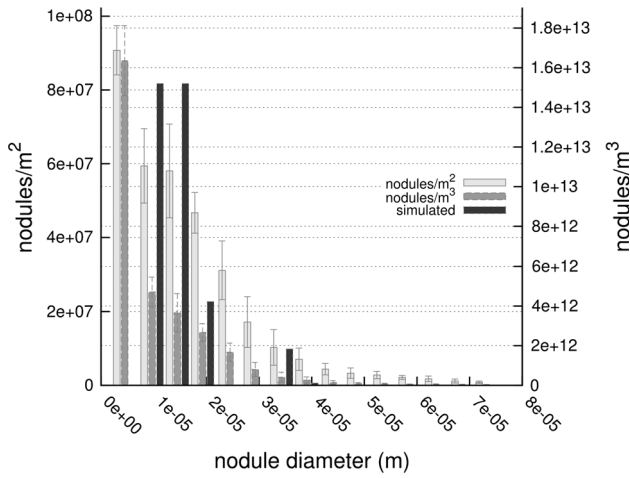
Fig. 18—Comparison of simulated and experimental discrete size distribution of graphite spheroids per unit area and volume (according to the classes listed in Table II) at the central zone of the specimen.
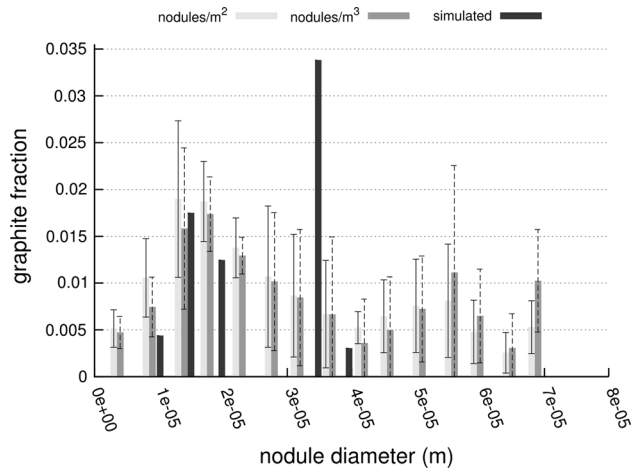

Fig. 20—Comparison of simulated and experimental discrete distribution of graphite fraction.
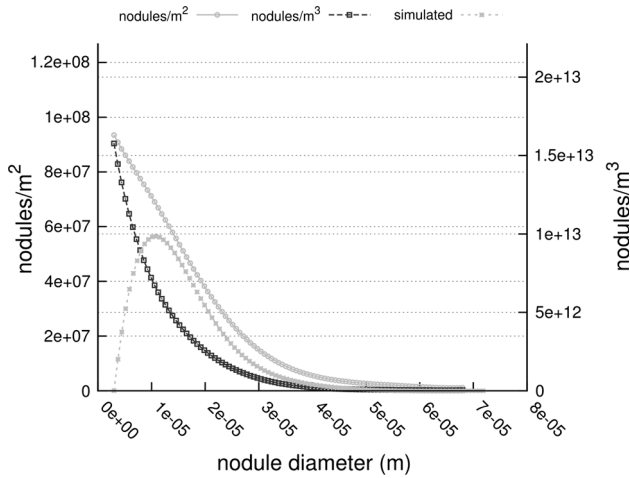

Fig. 19—Comparison of simulated and experimental continuous size distribution of graphite spheroids per unit area and volume at the central zone of the specimen.
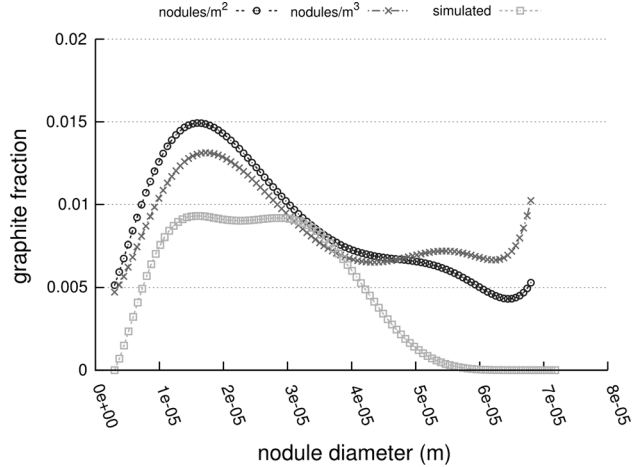

Fig. 21—Comparison of simulated and experimental continuous distribution of graphite fraction from Fig. 20.

composition is indicated by the values in Table II of cast alloy). The two peaks in the simulations tend to merge because the second peak has shifted towards a mean value of diameters due to the peak associated with class 7 in Figure 20.

Figure 22 shows good agreement between experiments and computations of discrete accumulated distribution fractions of graphite at the center of the specimen, except for the values of class 7 in the curve of computational results. This can be better observed in Figure 23, which shows continuous distributions of accumulated graphite fraction associated with the discrete distributions shown in Figure 22.

Graphite fractions obtained from the experimentally measured size distribution of graphite spheroids per unit area and volume and from simulation at the center of the part are plotted in Figure 24. Good agreement may be observed between experiments and simulations.
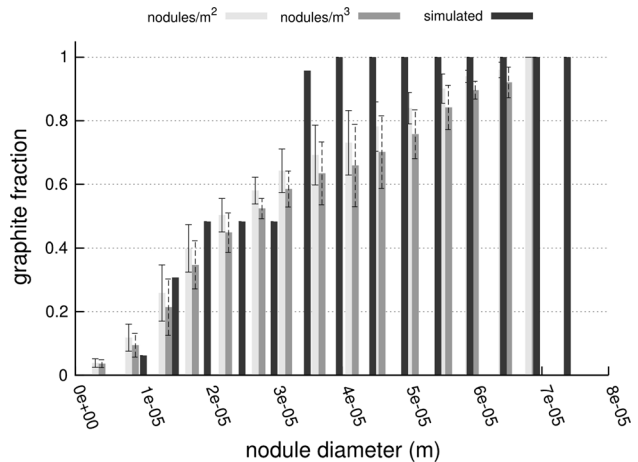

Fig. 22—Experimental and simulated discrete accumulated graphite fraction at the central zone of the specimen.
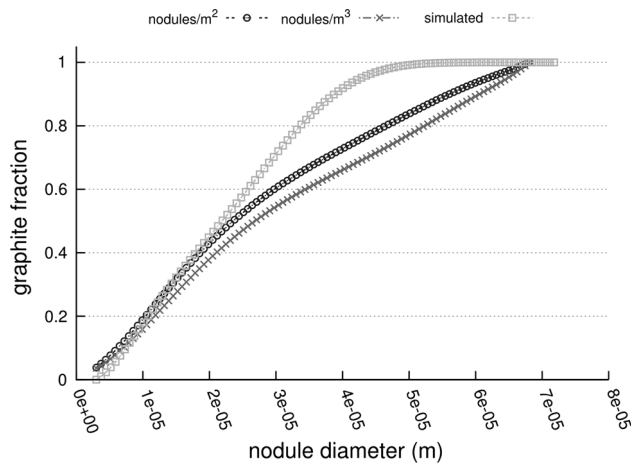
Fig. 23—Experimental and simulated continuous accumulated graphite fraction at the central zone of the specimen.
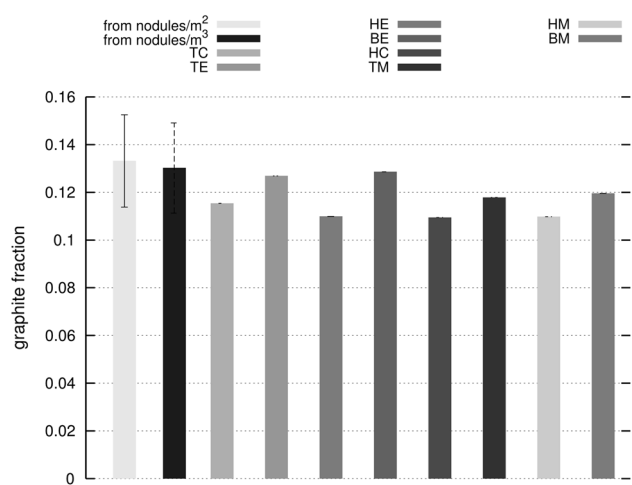

Fig. 24—Comparison of experimental (at the central zone of the specimen) and simulated (for eight nodes shown in Fig. 8(b)) graphite fraction.

VIII. CONCLUSIONS

A new thermo-metallurgical model has been reported in this paper, which is fully coupled from the point of view of micro-modeling and takes into account nucleation and growth of graphite spheroids along the entire cooling process. There are conceptual and methodological contributions in this formulation which apply to the study of nucleation and subsequent growth of graphite spheroids in cast irons. This may improve understanding and validations of theoretical formulations concerning the role played by chemical composition and heterogeneities in diffusive phase transformations that follow solidification, for continuous cooling processes as well as in processes under isothermal or controlled cooling.

For the first time, the influence of Si on phase changes at solid states from solidification has been taken into account using a macro–micro approach. This is important because the weight percentages of the different components (not just Si) at the end of solidification change between the first and last regions to freeze. Such differences in weight percentage of Si are associated with a retarded nucleation process between the stable and metastable eutectoid, among other consequences. Thus, by coupling the microstructural models of phase change in solid state with results from the microstructural model of solidification based in a divorced eutectic, it is possible to take into account heterogeneities in components at micro level. This seems to be a crucial feature required by predictive models which aim to run independently of experiments.

Regarding the stage of growth of spheroids from the end of solidification up to a temperature $T_{a_T}^\alpha$, this new model allows understanding the phenomenon that takes place during the phase changes in thermo-metallurgical processes with cooling interruptions, such as continuous-isothermal cooling processes or heat treatment processes. An interruption during a cooling process produces carbon accumulation in zones of austenite away from the interphase with graphite, thus promoting the formation of cementite or highly distorted austenite by the presence of carbon atoms dissolved in an FCC iron among other problems. A similar analysis may be conducted for isothermal processes in the intercritical stable eutectoid.

The importance of the characteristics of thermal evolution of a part or of locations of a part having different cooling rates was highlighted. If the cooling rate becomes high, the carbon content of austenite at the interphase with graphite at the start of the stable eutectoid phase change will be low; this is due to the longer time that carbon has to diffuse towards the spheroids, thus reducing carbon in the solid solution in austenite, decreasing the driving force for carbon diffusion during this stage. Low cooling rate, on the other hand, may cause or promote carbon accumulation in austenite at the interphase with graphite to the extent of having cementite nucleation. These are only two examples that illustrate the need to identify the percentages of the final number of graphite associated to each of the three stages considered, as well as the importance, the degree of dependence, and the influence that a phase change has on the subsequent ones.

The theoretical developments, as well as the computational results, represent advances with respect to the present state of the art in models, theoretical formulations, and phenomenological descriptions of the growth of graphite spheroids. Not only is it possible to know about the final graphite fraction, but it can also be characterized and serve to perform parametric studies in chemical composition, size and type of molds, geometry of the cast part, *etc.*, thus increasing the information which may be extracted at a micro level. Both aspects have different technological implications.

The final graphite fractions computed at zones in a part having several cooling rates are encouraging. The shape of the distribution of the graphite number per unit volume shows agreement with experiments (with one exception, *i.e.*, the number of spheroids for class 7), as well as the graphite fraction distributions and the accumulated graphite fraction.

$$C_C^{\alpha/\gamma} = 1.92 \times 10^{-3} - 1.59 \times 10^{-2}C_{Si} - 4.12$$
$$\times 10^{-6}T - 2.62 \times 10^{-3}(C_{Si})^2 + 2.31$$
$$\times 10^{-9}T^2 + 2.5 \times 10^{-5}C_{Si}T$$

$$C_C^{\gamma/\alpha} = 1.29 \times 10^{-1} + 5.13 \times 10^{-3}C_{Si}$$
$$- 2.56 \times 10^{-4}T + 2.9 \times 10^{-4}(C_{Si})^2$$
$$+ 1.24 \times 10^{-7}T^2 + 3.27 \times 10^{-4}C_{Si}T$$

$$T_{a_T}^{\alpha} = -\left(\sqrt{1.10 \times 10^{11} + 2.74 \times 10^{35}(C_{Si})^2 - 3.25 \times 10^{35}C_{Si} + 1.46 \times 10^{34}} + 1.74 \times 10^{23}C_{Si} - 1.02 \times 10^{23}\right)/8.53 \times 10^{19}$$

$$T_{A_1}^{\alpha} = -\left(\sqrt{3.47 \times 10^{11} + 1.60 \times 10^{22}(C_{Si})^2 - 2.19 \times 10^{21}C_{Si} + 5.85 \times 10^{19}} + 7.4 \times 10^{16}C_{Si} - 9.85 \times 10^{15}\right)/7.69 \times 10^{12}$$

APPENDIX A: PHASE DIAGRAMS

The equilibrium carbon concentrations for eutectoid phase changes together with the lower and upper bounds of the intercriticals stable and metastable eutectoid of the Fe-C-Si and Fe-Fe$_3$C-Si systems are as follows:

- Fe-C-Si:

$$C_C^{\gamma/g} = 1.60 \times 10^{-3} + 8.13 \times 10^{-5}C_{Si} - 6.46$$
$$\times 10^{-6}T + 5.47 \times 10^{-6}(C_{Si})^2$$
$$+ 1.85 \times 10^{-8}T^2 - 1.05 \times 10^{-4}C_{Si}T$$

- Fe-Fe$_3$C-Si:

$$C_C^{\gamma/\theta} = -7.34 \times 10^{-3} + 1.82 \times 10^{-1}C_{Si} + 1.7$$
$$\times 10^{-6}T + 2.92 \times 10^{-2}(C_{Si})^2$$
$$+ 1.72 \times 10^{-8}T^2 + 4.17 \times 10^{-5}C_{Si}T$$

$$C_C^{\alpha/\theta} = 2.99 \times 10^{-3} + 1.37 \times 10^{-4}C_{Si} - 9.84$$
$$\times 10^{-6}T + 1.10 \times 10^{-5}(C_{Si})^2 + 8.23$$
$$\times 10^{-9}T^2 - 1.89 \times 10^{-6}C_{Si}T$$

$$T_{a_T}^{P} = -\left(\sqrt{2.16 \times 10^{10} + 5.07 \times 10^{20}(C_{Si})^2 - 3.94 \times 10^{20}C_{Si} + 5.23 \times 10^{19}} + 3.08 \times 10^{15}C_{Si} - 2.82 \times 10^{15}\right)/2.32 \times 10^{12}$$

$$T_{A_1}^{P} = -\left(\sqrt{4.05 \times 10^{11} + 6.72 \times 10^{21}(C_{Si})^2 - 7.3 \times 10^{20}C_{Si} + 7.5 \times 10^{19}} + 5.46 \times 10^{16}C_{Si} + 1.16 \times 10^{16}\right)/2.4 \times 10^{13},$$

$$C_C^{\alpha/g} = -9.53 \times 10^{-4} + 1.02 \times 10^{-2}C_{Si} + 1.55$$
$$\times 10^{-6}T + 9.59 \times 10^{-4}(C_{Si})^2 + 1$$
$$\times 10^{-10}T^2 - 1.76 \times 10^{-5}C_{Si}T$$

where C_{Si} is the Si content in austenite at different interfaces expressed in weight percentage and T is the temperature of the alloy in Celsius degrees.

APPENDIX B: SURFACE OF SPHEROIDS IN CONTACT WITH FERRITE AND AUSTENITE

For the jth spheroid, the surfaces of graphite spheroids in contact with ferrite and austenite are given as fraction:

$$A_{\alpha/g_j} = \frac{\sum_{i=1}^{n_f} \left(R_{\alpha_i}\right)^2}{4\left(R_{g_j}\right)^2}, \qquad [B1]$$

$$A_{\gamma/g_j} = 1 - A_{\alpha/g_j}$$

where n_f is the number of ferrite grains nucleated on each graphite spheroid (see Table B-IV) and R_{α_i} is the radius of ferrite grains nucleated on the spheroid. A_{α/g_j} could be computed with higher precision by means of a surface integral and assuming that each ferrite grain is located on the spheroid; however, the differences with the results of Eq. [B1] are negligible.

APPENDIX C: VOLUME FRACTION OF GRAPHITE AND AUSTENITE

With the radius increment of graphite spheroid in a time integration interval Δt, $t + \Delta t$, the radius of a graphite spheroid corresponding to nucleation event j at time $t + \Delta t$ ($^{t+\Delta t}R_{g_j}$) is

$$^{t+\Delta t}R_{g_j} = {}^{t}R_{g_j} + \Delta R_{g_j}.$$

The value of ΔR_{g_j} is obtained from the differential Eqs. [6], [7], [9], or [10], depending on the temperature of the alloy and on the characteristics of the transformations.

With the values of radius of graphite spheroids, the graphite volume fraction is obtained from

$$f_g = \frac{4}{3}\pi \sum_{j=1}^{k} N_{g_j}^{V}\left(R_{g_j}\right)^3,$$

where k is the number of events of nucleation of graphite spheroids and $N_{g_j}^{V}$ the number of graphite spheroids per unit volume associated with the j event of nucleation.

As the austenite fraction is transformed into graphite, ferrite, and/or pearlite, its value should be computed again as

$$f_\gamma = \left(1 - f_g - f_\alpha - f_P\right),$$

where f_α and f_P are the volume fractions of ferrite and pearlite, respectively.

Details of the microstructure models from which f_α and f_P are calculated are given by Carazo.[12]

APPENDIX D: CARBON QUANTITY IN AUSTENITE

The value of C_C^γ per unit volume of RVE is computed as

Table B-IV. Thermo-physical Properties and Material Parameters of Cast Iron

Thermal Conductivity (W/mK)		Specific Heat (J/kg)	
Temperature [K (°C)]	Conductivity	Temperature [K (°C)]	C_P
553 (280)	54.1	293 (20)	500×10^3
693 (420)	38.1	873 (600)	750×10^3
833 (560)	47.1	1073 (800)	750×10^3
973 (700)	43.6	1418 (1145)	820×10^3
1113 (840)	38.1	1428 (1155)	840×10^3
1253 (980)	32.5	1673 (1400)	840×10^3
1393 (1120)	28.8		
1673 (1400)	45		
Mass density (kg/m³)	7300		
Solidification phase-change model[11]			
Eutectic latent heat	(J/kg)	2×10^5	
Carbon diffusion coefficient in liquid and austenite	(m²/s)	$D_C^l = 5 \times 10^{10}$ and D_C^{γ}[10]	
Graphite nucleation coefficients	$b^M = 1 \times 10^{13}$ (grains/m³ Ks)	$c^M = 280$ () (K)	
Graphite initial radius	(m)	$R_g^0 = 5.0 \times 10^{-7}$	
Austenite nucleation coefficient	(grains s/m³ K)	$A_\gamma = 1 \times 10^7$	
Gibbs–Thompson coefficient	(Km)	$\Gamma_{GT} = 2 \times 10^{-7}$	
Graphite and austenite densities	(kg/m³)	$\rho_g = 2023$ and $\rho_\gamma = 7000$	
Solid-state phase-change model[12]			
Initial thickness of the boundary layer ahead of the front of transformation (m)	$\delta = 5 \times 10^{-10}$[52]		
Ferrite latent heat	(J/kg)	6×10^4	
Initial numbers of ferrite grains	(grains)	$n_\alpha = 9$	
Initial radius of ferrite grains	(m)	$R_\alpha^0 = 1 \times 10^{-8}$	
Pearlite latent heat	(J/kg)	9×10^4	
Pearlite nucleation coefficient	(grains s/m³ K)	$\mu_P = 1 \times 10^{10}$	
Carbon diffusion coefficient in austenite and austenite/pearlite interface	(m²/s)	D_C^{γ}[10] and D_C^{B}[53]	
Enthalpy change during austenite–pearlite transformation	(J/kg)	ΔH_V^{P}[53]	
Interfacial free energy in ferrite at interface with cementite	(J/m²)	$\sigma^{\alpha/\theta}$[54]	

$$
{}^{t+\Delta t}C_C^{\gamma} = \frac{{}^{t}C_C^{\gamma}\rho_{\gamma}\left(1 - {}^{t}U_g - {}^{t}U_{\alpha} - {}^{t}U_P\right) + C_g\rho_g\left({}^{t}U_g - {}^{t+\Delta t}U_g\right) + C_{\alpha_C}\rho_{\alpha}\left({}^{t}U_{\alpha} - {}^{t+\Delta t}U_{\alpha}\right) + C_{P_C}\rho_P\left({}^{t}U_P - {}^{t+\Delta t}U_P\right)}{\rho_{\gamma}\left(1 - {}^{t+\Delta t}U_g - {}^{t+\Delta t}U_{\alpha} - {}^{t+\Delta t}U_P\right)}, \quad [\text{D1}]
$$

where C_{X_C}, ρ_X, and ${}^{t}U_X$ are carbon concentrations in weight percentage, density, and carbon quantity in a micro-constituent X, respectively. X may be austenite, graphite, ferrite, or pearlite. The derivation of Eq. [D1] may be seen in Carazo.[12]

APPENDIX E: THERMO-PHYSICAL PROPERTIES AND MATERIAL PARAMETERS USED IN THE NUMERICAL SIMULATIONS

Tables B-IV and E-V show the values of coefficients and thermo-physical properties of the alloy and sand used in the numerical simulation. The initial temperature of alloy is the same as the maximum value recorded in the experiments: 1478 K (1205 °C). The initial temperature for the cylindrical cup is the environmental temperature at the moment of conducting the experiments: 293 K (20 °C).

The values of specimen–mold conductance coefficient, specimen–environment and mold–environment convection heat transfer coefficients, and specimen thermocouple conductance coefficient are shown in Tables E-VI, E-VII, and E-VIII, respectively.

Table E-V.   Thermo-physical Properties of Sand

Temperature [K (°C)]	Thermal Conductivity (W/mK)
373 (100)	0.54
573 (300)	0.57
773 (500)	0.65
973 (700)	0.79
1173 (900)	1.00
1373 (1100)	1.26
1573 (1300)	1.59
1673 (1400)	1.59
Mass density (kg/m^3)	1550
Specific heat (J/kg)	1×10^6

Table E-VI.   Specimen–Mold Conductance Coefficient

Temperature [K (°C)]	Conductance Coefficient (W/m^2 K)
293 (20)	60
773 (500)	70
1123 (850)	90
1443 (1170)	100
1673 (1400)	100

Table E-VII.   Specimen–Environment and Mold–Environment Convection Heat Transfer Coefficients

Temperature [K (°C)]	Heat Transfer Coefficient (W/m^2 K)
293 (20)	50
1673 (1400)	80

Table E-VIII.   Specimen–Thermocouple Conductance Coefficient

Interface	Heat Transfer Coefficient (W/m^2 K)
Part-thermocouple	40

REFERENCES

1. ASTM A247-10: *ASTM International*, West Conshohocken, PA, 2010. doi:10.1520/A0247-10.
2. D.M. Stefanescu and C.S. Kanetkar: in *Computer Simulation of Microstructural Evolution*, D.J. Srolovitz, eds., TMS, Warrendale, PA, 1985, pp. 171–88.
3. B.C. Liu, H.D. Zhao, W.Y. Liu, and D.T. Wang: *Int. J. Cast Met. Res.*, 1999, vol. 11 (5), pp. 471–76.
4. S. Chang, D. Shangguan, and D.M. Stefanescu: *AFS Trans.*, 1991, vol. 99, pp. 531–41.
5. S. Chang, D. Shangguan, and D.M. Stefanescu: *Metall. Trans. A*, 1992, vol. 23A, pp. 1333–46.
6. A. Almansour, K. Matsugi, T. Hatayama, and O. Yanagisawa: *Mater. Trans., JIM*, 1996, vol. 37(4), pp. 612–19.
7. D. Venugopalan: in *The Physical Metallurgy of Cast Iron. Proceedings of the Fourth International Symposium on the Physical Metallurgy of Cast Iron*, G. Ohira, T. Kusakawa, E. Niyama, eds., Materials Research Society, Tokyo, Japan, 1989, pp. 271–78.
8. D. Venugopalan: *Metall. Trans. A*, 1990, vol. 21A, pp. 913–18.
9. M. Wessen and I.L. Svensson: *Metall. Trans. A*, 1996, vol. 27A, pp. 2209–20.
10. J. Lacaze and V. Gerval: *ISIJ Int.*, 1998, vol. 38 (7), pp. 714–22.
11. P.M. Dardati: Ph.D. Thesis, Facultad de Ciencias Exactas Físicas y Naturales, Universidad Nacional de Córdoba, 2005.
12. F.D. Carazo: Ph.D. Thesis, Facultad de Ciencias Exactas Físicas y Naturales, Universidad Nacional de Córdoba, 2012.
13. D. Celentano, E. Oñate, and S. Oller: *Int. J. Num. Meth. Eng.*, 1994, vol. 37, pp. 3441–65.
14. R. Hill: *J. Mech. Phys. Solids*, 1965, vol. 13 (4), pp. 213–22.
15. F.D. Carazo, P.M. Dardati, D.J. Celentano, and L.A. Godoy: *Metall. Trans. B*, 2012, vol. 43B (6), pp. 1579–95, DOI:10.1007/s11663-012-9710-y.
16. B. Lux: *AFS Cast Met. Res. J.*, 1972, vol. 8 (1), pp. 25–38.
17. B. Lux: *AFS Cast Met. Res. J.*, 1972, vol. 8 (2), pp. 49–65.
18. D.M. Stefanescu and D.K. Bandyopadhyay: in *The Physical Metallurgy of Cast Iron. Proceedings of the Fourth International Symposium on the Physical Metallurgy of Cast Iron*, G. Ohira, T. Kusakawa, E. Niyama, eds., Materials Research Society, Tokyo, Japan, 1989, pp. 15–26.
19. J.A. Sikora, G.L. Rivera, and H. Biloni: in *F. Weinberg Int. Symp. on Solidification Processing*, J.E. Lait and I.V. Samarasekera, eds., Pergmon Press, Inc., New York, NY, 1990, pp. 280-88.
20. D.K. Banerjee and D.M. Stefanescu: *AFS Trans.*, 1991, vol. 99, pp. 747–59.
21. Z. Jiyang: *Acta Metall. Sin.*, 1989, vol (4), pp. 261–65.
22. D.M. Stefanescu: *J. Mater. Sc. Eng. A*, 2005, vols. 413–414, pp. 322–33.
23. R.W. Cahn and P. Haasen (eds.): Physical Metallurgy, vol. 1, 4th ed., Elsevier, Amsterdam, The Netherlands, 1996, p. 767.

24. W. Kurz and D.J. Fisher: *Fundamentals of Solidification*, 1st ed., Trans. Tech. Public, Switzerland, 1984, p. 98.
25. G. Lesoult, M. Castro, and J. Lacaze: *Acta Mater.*, 1998, vol. 46 (3), pp. 983–95.
26. K.C. Su, I. Ohnaka, I. Yamanuchi, and T. Fukusaco: in *The Physical Metallurgy of Cast Iron*, H. Fredriksson and M. Hillert, eds., Proc. Materials Research Society, Nort Holland, 1985, pp. 181–189.
27. E. Fras: in *The Physical Metallurgy of Cast Iron*, H. Fredriksson and M. Hillert, eds., Proc. Materials Research Society, Nort Holland, 1985, pp. 191–99.
28. H. Fredriksson and I.L. Svensson: in *The Physical Metallurgy of Cast Iron*, H. Fredriksson and M. Hillert, eds., Proc. Materials Research Society, Nort Holland, 1985, pp. 273–84.
29. M. Castro, P. Alexandre, J. Lacaze, and G. Lesoult: in *The Physical Metallurgy of Cast Iron. Proceedings of the Fourth International Symposium on the Physical Metallurgy of Cast Iron*, G. Ohira, T. Kusakawa, E. Niyama, eds., Materials Research Society, Tokyo, Japan, 1989, pp. 433–40.
30. E. Frás, W. Kapturkiewicz, and H.F. Lopez: *AFS Trans.*, 1992, vol. 100, pp. 583–91.
31. Y. Zhang, S.V. Subramanian, and G.R. Purdy: in *The Physical Metallurgy of Cast Iron*, G. Lesoult and J. Lacaze, eds., Trans. Tech. Public, Switzerland, 1994, pp. 461–68.
32. A. Almansour, K. Matsugi, T. Hatayama, and O. Yanagisawa: *Mater. Trans., JIM*, 1995, vol. 36(12), pp. 1487–95.
33. L. Wenzhen and L. Baicheng: in *Proceedings of the Technical Forum, 62nd World Foundry Congress*, American Foundrymen's Soc., Inc., Philadelphia, USA, 1996, pp. 2–10.
34. R. Aagaard, J. Hattel, W. Schafer, I.L. Svensson, and P.N. Hansen: *AFS Trans.*, 1996, vol. 104, pp. 659–67.
35. C. Charbon and M. Rappaz: *Adv. Mater. Res. (Durnten-Zurich, Switz.)*, 1997, vol. 4–5, pp. 453–60.
36. E. Frás, W. Kapturkiewicz, and A. Burbelko: *Adv. Mater. Res. (Durnten-Zurich, Switz.)*, 1997, vol. 4–5, pp. 499–504.
37. J. Liu and R. Elliot: *J. Cryst. Growth*, 1998, vol. 191, pp. 261–67.
38. J. Lacaze, M. Castro, and G. Lesoult: *Acta Mater.*, 1998, vol. 46 (3), pp. 997–1010.
39. I. Ohnaka: *Int. J. Cast Met. Res.*, 1999, vol. 11 (5), pp. 267–72.
40. M.I. OnsoØien, O. Grong, O. Gundersen, and T. Skaland: *Metall. Trans. A*, 1999, vol. 30A, pp. 1053–68.
41. J. Čech and L. Zemčík: *Solidif. Metals Alloys*, 2000, vol. 2(44), pp 39–44.
42. H. Zhao and B. Liu: *ISIJ Int.*, 2001, vol. 41 (9), pp. 986–91.
43. H. Zhao and B. Liu: *Int. J. Cast Met. Res.*, 2003, vol. 16 (13), pp. 281–86.
44. P.M. Dardati, L.A. Godoy, and D.J. Celentano: *J. Appl. Mech.*, 2006, vol. 73 (6), pp. 977–83.
45. R.W. Heine: *AFS Trans.*, 1986, vol. 94, pp. 391–402.
46. A. Hultgren: *Trans. ASM.*, 1947, vol. 39, pp. 915–89.
47. A. Fick: *Ann. Phys. (Berlin, Ger.)*, 1855, vol. 170(1), pp. 59–86.
48. P.G. Shewmon: *Diffusion in Solids*, 2nd ed., Wiley, New York, NY, 1989, p. 28.
49. M. Abramoff, P. Magalhaes, and S. Ram: *Biophotonics Int.*, 2004, vol. 11 (7), pp. 36–42.
50. C.A. Schneider, W.S. Rasband, and K.W. Eliceiri: *Nat. Methods*, 2012, vol. 9 (7), pp. 671–75, DOI:10.1038/nmeth.2089.
51. E.E. Underwood: *Quantitative Stereology*, 1st ed., Addison-Wesley, Reading, MA, 1970, p. 119.
52. D.M. Stefanescu: *Science and Engineering of Casting Solidification*, 2nd ed., Springer, New York, 2009, p. 21.
53. A.S. Pandit: Ph.D. Thesis, Department of Materials Science and Metallurgy, University of Cambridge, 2011.
54. J.J. Kramer, G.M. Pound, and R.F. Mehl: *Acta Metall.*, 1958, vol. 6 (12), pp. 763–71.